Research on Engineering Structures & Materials
www.jresm.org
Research Group

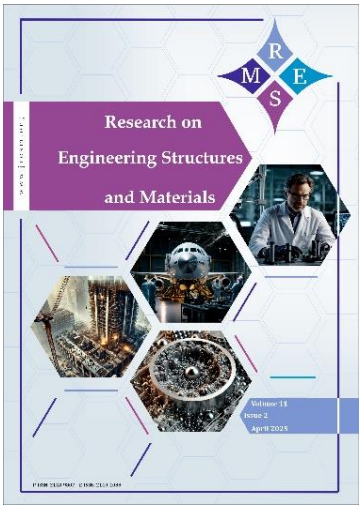

Linear forced vibration response of FG-BNNT/CF reinforced polymer matrix composite beams resting on viscoelastic foundations

Mehdi Billah Ouassim, Mustapha Fouaidi, Laidi Zahiri, Naoual Belouaggadia

Online Publication Date: 20 November 2025

URL: http://www.jresm.org/archive/resm2025-1075me0810rs.html
DOI: http://dx.doi.org/10.17515/resm2025-1075me0810rs

Journal Abbreviation: *Res. Eng. Struct. Mater.*

To cite this article
Ouassim M B, Fouaidi M, Zahiri L, Belouaggadia N. Linear forced vibration response of FG-BNNT/CF reinforced polymer matrix composite beams resting on viscoelastic foundations. *Res. Eng. Struct. Mater.*, 2026; 12(3): 1677-1702.

Research on Engineering Structures & Materials
www.jresm.org
Research Group

Research Article

Linear forced vibration response of FG-BNNT/CF reinforced polymer matrix composite beams resting on viscoelastic foundations

Mehdi Billah Ouassim [*,1,a], Mustapha Fouaidi [1,2,b], Laidi Zahiri [1,c], Naoual Belouaggadia [1,d]

[1]*Laboratory of Modelling and Simulation of Intelligent Industrial Systems (M2S2I) ENSET, Hassan II University of Casablanca, Morocco*
[2]*Mechanical and Energy (ME) group, LPNAMME laboratory, Department of Physics, Faculty of Sciences, Chouaib Doukkali University, P.B 20, 24000 El Jadida, Morocco*

Article Info

Article History:

Received 10 Aug 2025
Accepted 12 Nov 2025

Keywords:

Nanocomposites; Forced vibration; Visco-Winkler-Pasternak foundation; Finite element method; Newmark time scheme

Abstract

This paper aims to analyze the forced vibration (FV) behavior of polymer matrix (PM) composite material beams (PMCBs), incorporating functionally graded boron nitride nanotubes (FG-BNNT) and carbon fibers (CF) reinforcements, supported on viscoelastic foundations (VEFs). The PMCBs are subjected to dynamic mechanical loading (DMLs) under various boundary conditions (BCs). The viscoelastic foundations supporting the PMCBs are used to simulate the interaction between the composite beams and their surrounding media. The Visco-Winkler-Pasternak (VWP) elastic foundation model is adopted to represent these foundations. The structural behavior of PMCBs is analyzed based on the first-order shear deformation theory (FSDT). The effective material properties are determined through a combination of the modified Halpin-Tsai model (MHTM), the rule of mixtures (ROM), and a fiber micromechanics method (FMM). The governing equations of motion are derived using Hamilton's principle (HP) and solved numerically via the finite element method (FEM) combined with the Newmark implicit time integration numerical method (NITINM). After validation studies, parametric analyses are conducted to analyze the impact of multiple factors on the dynamic behavior of FG-BNNT/CF-reinforced PMCBs. This study highlights the vibration behavior of advanced composite structures and their potential use in designing and controlling smart materials and structures.

1. Introduction

The vibrational behavior of structural elements, such as beams made from advanced composite materials under dynamic loads and resting on viscoelastic foundations, can be observed in various engineering applications [1-2], including the manufacturing of aircraft components, building foundations, automotive suspension systems, and many others. Particularly in the modeling of turbine blades in aircraft engines [3], they are subjected to extreme operating conditions, including high vibrations, thermal loads, and significant mechanical dynamic loads [8]. Moreover, significant efforts have been devoted to the analysis of the vibrational characteristics of plates and beams with varying boundary conditions and geometric parameters [9].

Nanocomposites represent an advanced class of composite materials [10], consisting of a matrix reinforced with nanoscale fillers [11]. However, their primary challenge lies in the dispersion and agglomeration of the nanofillers within the matrix [12]. Due to their small size, these fillers tend to

*Corresponding author: mehdibillah1@gmail.com
[a]orcid.org/0009-0006-6108-3104; [b]orcid.org/ 0000-0003-1675-8513; [c]orcid.org/ 0000-0003-2685-6088; [d]orcid.org/ 0000-0001-9313-2974
DOI: http://dx.doi.org/10.17515/resm2025-1075me0810rs

cluster, leading to an uneven distribution throughout the composite material, which may significantly degrade its mechanical performance. To overcome the problem of filler agglomeration, reinforcements are applied simultaneously at both macro and nanoscale levels [9]. The integration of reinforcement elements across multiple scales in these composite materials can greatly enhance their mechanical and functional performance. In the literature, such materials are commonly known as multi-scale hybrid composites [10].

Multi-scale hybrid composites represent an emerging class of materials, with their mechanical response to various loading conditions having been extensively studied over the past decade [11-13]. He et al. [14] investigated the nonlinear free and forced vibration characteristics of laminated multiscale composite beams reinforced with carbon nanotubes (CNTs) and carbon fibers (CF) embedded in a polymer matrix, within the framework of the classical beam theory. Ahmadi et al. [15] investigated the bending, buckling, and free vibration of hybrid composites with a polymer matrix reinforced with CF/CNT using FEM. In a related investigation, Ebrahimi and Dabbagh [16] analyzed the vibrational response of multiscale hybrid nanocomposite plates employing the Halpin Tsai model. Their findings revealed that such hybrid configurations exhibit enhanced natural frequencies compared to conventionally reinforced composite counterparts.

Carbon-based fillers such as carbon nanotubes, graphene nanoplatelets, and graphene oxide powders are the most commonly used for matrix reinforcement in nanocomposites and multi-scale hybrid composites. Recently, boron nitride nanotubes (BNNTs) have emerged as promising alternative nanoscale fillers. BNNTs are a novel type of advanced reinforcement with advantageous applications in polymer nanocomposites, owing to their chemical compatibility with polymers and their remarkable mechanical, thermal, magnetic, and electrical properties. These nanotubes enhance the tensile strength, modulus of elasticity, and thermal properties of polymer nanocomposites. In addition, BNNTs are highly attractive as a nanofiller for high-temperature integrated and structural applications due to their extreme thermal stability and excellent mechanical properties [17]. Despite the numerous advantages of BNNTs, their integration with carbon fibers remains limited. Therefore, one of the objectives of this work is to combine BNNTs with carbon fibers to enhance the mechanical properties of matrix materials.

In many real-world applications, polymer matrix composite beams PMCBs interact with surrounding materials. Therefore, for effective maintenance and optimal production of PMCBs, it is essential to consider the effects of these interactions with a viscoelastic medium. Various foundation models have been proposed to simulate the interaction between PMCBs and viscoelastic foundations. The earliest model is the Winkler-type viscoelastic foundation. A more advanced model is the Pasternak-type viscoelastic foundation, which accounts for the interaction between discrete springs, unlike the Winkler model. The study of the mechanical behavior of PMCBs resting on elastic and viscoelastic foundations has garnered significant attention [18 -21].

The existing literature on the dynamic response of two-phase and three-phase carbon-based composite beams has predominantly focused on systems reinforced with carbon nanotubes (CNTs) and graphene platelets (GPLs) as nanoscale fillers, combined with carbon fibers (CFs) as macroscale reinforcements. However, only a limited number of studies have investigated the influence of viscoelastic foundations on the dynamic behavior of such nanocomposites. Moreover, recent findings have highlighted the limitations inherent in relying solely on carbon-based fillers, motivating the exploration of alternative nanostructures with superior mechanical and thermal characteristics. Among the reviewed works, most have concentrated on plate structures, leaving beam configurations comparatively underexplored.

In light of these gaps, investigating the dynamic response of composite structures reinforced with CFs in combination with alternative nanoscale fillers emerges as a promising and novel research direction. Accordingly, the primary objective of the present study is to analyze the dynamic response of functionally graded (FG) boron nitride nanotube (BNNT)/CF-reinforced polymer matrix composite beams resting on viscoelastic foundations under dynamic loading. In this work, the first-order shear deformation theory (FSDT) is used for structural modeling of PMCBs. The effective material properties are determined through the modified Halpin-Tsai model (MHTM) and the rule of mixtures (ROM), combined with a fiber micromechanics method (FMM). The equations

of motion are derived using Hamilton's principle (HP) and are solved using the finite element method (FEM) along with the Newmark-β method. To the best of the authors' knowledge, no previous work has addressed the integration of FG-BNNTs with CFs as hybrid reinforcements in composite beams supported by viscoelastic foundations and subjected to dynamic excitation. The present work distinguishes itself through the following key contributions:

- Integration of functionally graded boron nitride nanotubes (FG-BNNTs) and carbon fibers (CFs) within a polymer matrix to achieve a multi-scale reinforcement architecture.
- Comprehensive analysis of the linear vibration response of the composite beams under dynamic loading for various boundary conditions.
- Advanced modeling of the viscoelastic foundation using the Pasternak-type formulation, incorporating both shear layer effects and damping characteristics.
- Hybrid use of micromechanical modeling and the finite element method (FEM) to determine the effective material properties and evaluate the structural response with high fidelity.

The remainder of this paper is structured as follows. Section 2 presents a comprehensive mathematical formulation of the problem under consideration. In section 3, the numerical solution strategy is elaborated, employing the FEM in conjunction with the NITINM scheme. Section 4 is devoted to the validation of the developed numerical model, followed by an in-depth parametric analysis. Finally, Section 5 concludes the study by summarizing the principal findings and insights.

2. Mathematical Formulation

To further highlight these contributions and position the present study within the existing body of research, a comparative synthesis is provided in Table 1. The table highlights the main types of reinforcements, foundations, methods, analyzed vibration types, and limitations or gaps of previous studies

Table 1. Comparison of existing studies on multi-scale hybrid composite beams and the present work.

Reference	Type of Reinforcement	Foundation Model	Theory / Method	Type of Vibration Analyzed	Main Limitation / Research Gap
He et al. [10]	CNT + CF (multi-scale)	No foundation	Classical Beam Theory	Free and forced nonlinear vibration	Excludes BNNT reinforcement and viscoelastic effects
Ebrahimi & Dabbagh [9]	CNT + CF + viscoelastic phase	Viscoelastic	Refined Beam Theory	Free vibration	No FG-BNNTs or graded material distribution
Yang et al. [17]	Homogeneous material	Viscoelastic	Timoshenko Beam Theory	Dynamic response to moving load	No composite reinforcement or FG concept
Abdollahi & Yas [21]	BNNT reinforced polymer	Elastic	Timoshenko Beam Theory	Free vibration	No hybrid CF/BNNT reinforcement or viscoelastic foundation
Merzouki et al. [3]	FG porous nanocomposite	Elastic	Trigonometric shear deformation beam theory	Linear vibration	Focus on nonlocal effects, not viscoelastic damping

Reference	Type of Reinforcement	Foundation Model	Theory / Method	Type of Vibration Analyzed	Main Limitation / Research Gap
Present work	CF + FG-BNNT hybrid nanocomposite	Viscoelastic	Timoshenko Beam Theory	Linear forced vibration under various BCs	Introduces multi-scale FG-BNNT/CF hybridization and advanced viscoelastic foundation modeling

2.1. Problem Description

The structures considered in this examination are straight, slender composite beams with length L, and rectangular cross-sections of area S = b × h where b, and h represent the width and thickness of the beams, respectively. The composite beams under study are assumed to be subjected to transverse sudden dynamic loads $p_z = p_3(x,t)$ with various boundary conditions. These beams are supported by viscoelastic foundations ($VEFs$), modeled using the Visco-Winkler-Pasternak (VWP) elastic foundation model, which is characterized by the material properties K_w,K_p, and D_c, as shown in Fig.1.

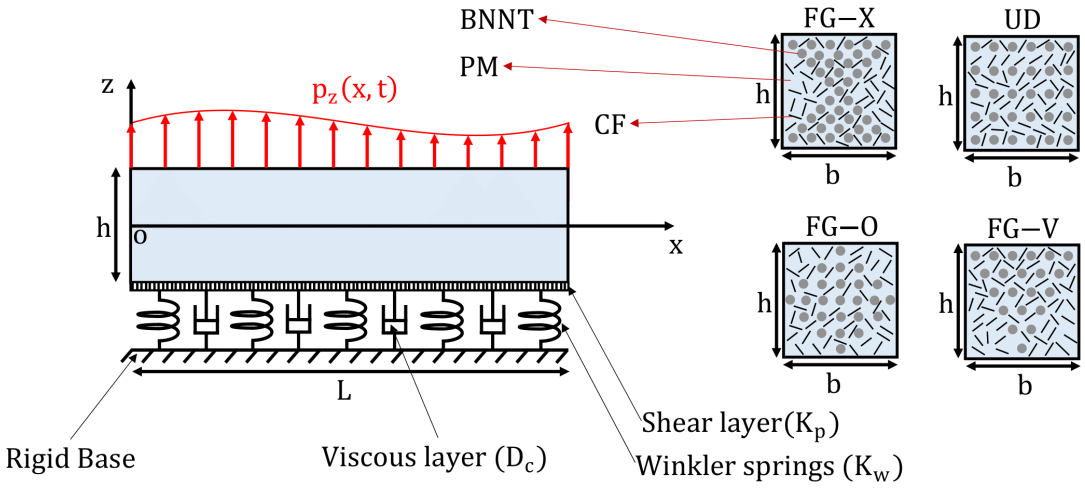

Fig. 1. Geometry of FG-BNNT/CF-reinforced polymer matrix composite beams supported by viscoelastic foundations, featuring various BNNT reinforcement patterns and subjected to external transverse dynamic loads and boundary conditions (right), and polymer matrix cross-sections with hybrid FG-BNNT and CF fillers (left)

The composite beams analyzed in this study are made of a polymer matrix (PM) material reinforced with a combination of both macro-sized carbon fiber (CF) reinforcements and nano-sized BNNT fillers, as shown in Fig. 1. The BNNT distribution is assumed to follow different functional grading patterns, such as (FG-V-BNNT), (FG-O-BNNT), and (FG-X-BNNT), as well as a uniform distribution (UD-BNNT) across the composite beam's thickness. The CF fillers are considered to be uniformly dispersed (UD) within the polymer matrix.

2.2. Material Properties of the FG-BNNT/CF Reinforced PM Composite Beams

A homogenization procedure (HP) is utilized to determine the effective material properties of the structure under investigation, as shown in Fig. 2. The homogenization procedure used is developed through a two-step process, integrating a modified Halpin-Tsai model [22-23] with a fiber micromechanical approach [24].

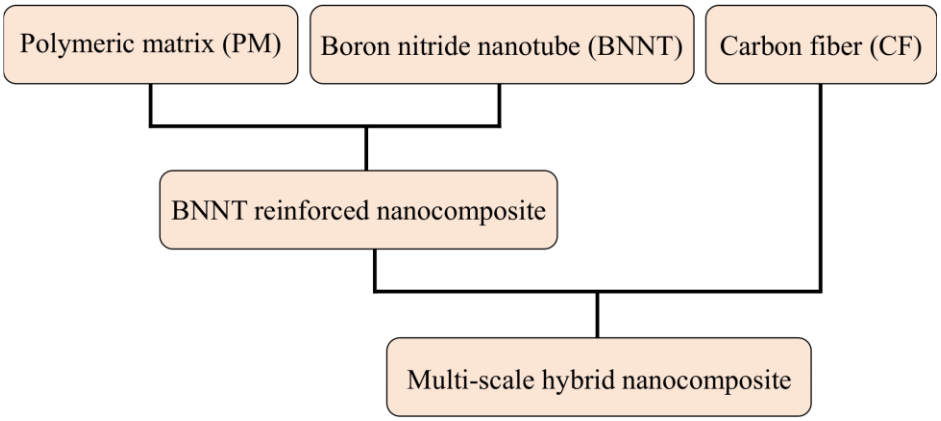

Fig. 2. Flowchart depicting the arrangement of materials in the formation of multi-scale hybrid nanocomposites

2.2.1 Modified Halpin-Tsai Model for Predicting BNNT/PM Material Properties

Using the modified Halpin-Tsai model, the effective Young's modulus $E_{BNNT/PM}(z)$ of the FG-BNNT-reinforced PM is given as follows:

$$E_{BNNT/PM}(z) = \alpha_L E_L(z) + \alpha_T E_T(z) \tag{1}$$

Here, $\alpha_L = 3/8$ and $\alpha_T = 1 - \alpha_L$, where $E_L(z)$ and $E_T(z)$ represent the axial and transverse Young's moduli of the FG-BNNT-reinforced PM, respectively. They are calculated as follows:

$$E_L(z) = \frac{1 + \xi_L \eta_L V_{BNNT}(z)}{1 - \eta_L V_{BNNT}(z)} E_{PM} \; ; \; E_T(z) = \frac{1 + \xi_T \eta_T V_{BNNT}(z)}{1 - \eta_T V_{BNNT}(z)} E_{PM} \tag{2}$$

With η_L and η_T are given by:

$$\eta_L = \frac{(E_{BNNT}/E_{PM}) - 1}{(E_{BNNT}/E_{PM}) + \xi_L} \; ; \; \eta_T = \frac{(E_{BNNT}/E_{PM}) - 1}{(E_{BNNT}/E_{PM}) + \xi_T} \tag{3}$$

In which E_{PM}, and E_{BNNT} represent the Young's moduli of the PM material and BNNT nanofillers, respectively. The geometric parameters ξ_L and ξ_T are determined as follows:

$$\xi_L = 2\beta_L \; ; \; \xi_T = 2 \tag{4}$$

Where β_L refers to the filler's aspect ratio determined as $\beta_L = \frac{L_{BNNT}}{d_{BNNT}} = 300$, with L_{BNNT} and d_{BNNT} representing the length and diameter of the BNNT fillers, respectively. The volume fraction $V_{BNNT}(z)$ for the four FG distribution patterns is calculated as follows:

$$V_{BNNT}(z) = \begin{cases} V^*_{BNNT} & \text{for (UD-BNT)} \\ \left(1 + \frac{2z}{h}\right) V^*_{BNNT} & \text{for (FG-V-BNT)} \\ 2\left(1 - \frac{2|z|}{h}\right) V^*_{BNNT} & \text{for (FG-O-BNT)} \\ 2\left(\frac{2|z|}{h}\right) V^*_{BNNT} & \text{for (FG-X-BNT)} \end{cases} \tag{5}$$

Where V^*_{BNNT} denotes the total volume fraction of BNNT, which can be approximated as:

$$V_{BNNT}^{*} = \frac{W_{BNNT}}{W_{BNNT} + (\rho_{BNNT}/\rho_{PM})(1 - W_{BNNT})} \tag{6}$$

In which ρ_{PM}, and ρ_{BNNT} represent the mass densities of the PM and BNNT reinforcements, respectively, and W_{BNNT} denotes the weight fraction of the BNNT. The effective Poisson's ratio $v_{BNNT/PM}(z)$ of the PMCBs is calculated using the ROM as follows:

$$v_{BNNT/PM}(z) = v_{BNNT}V_{BNNT}(z) + v_{PM}V_{PM}(z) \tag{7}$$

Where $V_{PM}(z)$ and $V_{BNNT}(z)$ denote the volume fractions of the PM and BNNT reinforcement, respectively. The volume fraction of the PM is provided by the following relation:

$$V_{PM}(z) = 1 - V_{BNNT}(z) \tag{8}$$

The mass density $\rho_{BNNT/PM}$ of the FG-BNNT reinforced PM composite beams is determined by:

$$\rho_{BNNT/PM}(z) = \rho_{BNT}V_{BNT}(z) + \rho_{PM}V_{PM}(z) \tag{9}$$

The effective shear modulus $G_{BNNT/PM}$ of the FG-BNNT-reinforced PM composite beams can be calculated as follows:

$$G_{BNNT/PM}(z) = \frac{E_{BNNT/PM}(z)}{2\big(1 + v_{BNNT/PM}(z)\big)} \tag{10}$$

2.2.2. Micromechanical Scheme for Determining the Material Properties Of FG-BNNT/CF Reinforced PM

The effective mechanical properties of the FG-BNNT/CF-reinforced PM are determined using the micromechanical approach as follows:

$$\begin{cases} E_{eff}(z) = V_{CF}(z)E_{CF} + V_{BNNT/PM}(z)E_{BNNT/PM}(z) \\ G_{eff}(z) = \left(\dfrac{V_{CF}(z)}{G_{CF}} + \dfrac{V_{BNNT/PM}(z)}{G_{BNNT/PM}(z)}\right)^{-1} \\ \rho_{eff}(z) = V_{CF}(z)\rho_{CF} + V_{BNNT/PM}(z)\rho^{BNNT/PM}(z) \\ v_{eff}(z) = V_{CF}(z)v_{CF} + V_{BNNT/PPM}(z)v_{BNNT/PM} \end{cases} \tag{11}$$

Where E, G, ρ denote the Young's modulus, shear modulus, Poisson's ratio, and mass density, respectively. In Eq. (11), the superscripts CF and BNNT/PM refer to carbon fiber and BNNT reinforced PM, respectively. Additionally, V_{CF} and $V_{BNNT/PM}$ represent the volume fractions of carbon fiber and the polymer matrix reinforced with signle walled BNNT, respectively, and they are related as follows:

$$V_{CF} + V_{BNNT/PM} = 1 \tag{12}$$

The material properties of the PM, BNNT, and CF are listed in Table 2.

Table 2. Material properties of the BNNT, PM, and CF [21, 22]

Parameter	Values
E_{PM}(GPa)	2.5
v_{PM}	0.3
ρ_{PM}(kg/m^3)	1190
E_{BNNT}(TPa)	1.064
v_{BNNT}	0.14
ρ_{BNNT}(kg/m^3)	2270
E_{CF}(GPa)	233.05
G_{CF}(GPa)	8.96
v_{CF}	0.2
ρ_{CF}(kg/m^3)	1750

2.3. Displacement Field

By applying the 1D-FSDT for beams, the displacement field at a given point (x, z) within the beam at time t can be expressed as:

$$\begin{cases} U_1 = u_1 + z\theta_1 \\ U_3 = u_3 \end{cases} \tag{13}$$

Here, U_1 and U_3 are the global displacements of the beam, while u_1, u_3, and θ_1 denote the mid-plane axial, vertical displacements, and rotation about the y-axis, respectively.

2.4. Strain Field

The vector of reduced strain for the FG-BNNT/CF-reinforced PMCBs is expressed as:

$$\begin{cases} \varepsilon_{11} = e_{11} + z\kappa_{11} \\ \gamma_{13} = \chi_{13} \end{cases} \tag{14}$$

Where e_{11}, κ_{11} and χ_{13} denote the generalized membrane strain, curvature strain, and transverse shear strain, respectively, and are defined as follows:

$$\begin{cases} e_{11} = \dfrac{\partial u_1}{\partial x} \\ \kappa_{11} = \dfrac{\partial \theta_1}{\partial x} \\ \chi_{13} = \dfrac{\partial u_3}{\partial x} + \theta_1 \end{cases} \tag{15}$$

2.5. Constitutive Equations

The vector of reduced stresses for the FG-BNNT/CF-reinforced PMCBs is described as:

$$\begin{cases} \sigma_{11} = Q_{11}\varepsilon_{11} \\ \tau_{13} = Q_{55}\gamma_{13} \end{cases} \tag{16}$$

Where σ_{11} and τ_{13} represent the axial stress and transverse shear stress, respectively. The formulas for the stiffness coefficients Q_{11} and Q_{55} are:

$$Q_{11} = \frac{E_{eff}}{1 - v_{eff}^2} \; ; \; Q_{55} = G_{eff} \tag{17}$$

The generalized membrane stress N_{11}, bending stress M_{11}, and transverse shear stress N_{13} are defined as follows:

$$\begin{cases} N_{11} = \int_{-b/2}^{b/2}\int_{-h/2}^{h/2}(\sigma_{11})dzdy = Ae_{11} + B\kappa_{11} \\ M_{11} = \int_{-b/2}^{b/2}\int_{-h/2}^{h/2}(z\sigma_{11})dzdy = Be_{11} + D\kappa_{11} \\ N_{13} = \int_{-b/2}^{b/2}\int_{-h/2}^{h/2}(\tau_{13})dzdy = S\chi_{13} \end{cases} \tag{18}$$

With, A, B, D, and S denote the axial, coupling, bending, and shear rigidities, respectively.

$$(A, B, S, D) = \int_{-b/2}^{b/2}\int_{-h/2}^{h/2}(Q_{11}, zQ_{11}, k_sQ_{55}, z^2Q_{11})dzdy \tag{19}$$

where $k_s = 5/6$ denotes the shear modification parameter.

2.6. Weak-Form Dynamical Equation

The equations of motion for the FG-BNNT/CF-reinforced PMCBs follow from Hamilton's principle [23]:

$$\int_{t_1}^{t_2}\left(\delta W_{int} + \delta W_f - \delta W_{ext} - \delta W_k\right)dt = 0 \tag{20}$$

where $W_{\text{int}}, W_f, W_{\text{ext}}$, and W_k denote the internal strain energy, foundation strain energy, external work, and kinetic energy of the FG-BNNT/CF beam, respectively, defined as:

$$\begin{cases} \delta W_{int} = \int_0^L (N_{11}\delta e_{11} + M_{11}\delta\kappa_{11} + N_{13}\delta\chi_{13})dx \\ \delta W_f = \int_0^L \int_{-b/2}^{+b/2}\left(u_3K_w\delta u_3 + \dfrac{\partial u_3}{\partial x}K_p\dfrac{\delta\partial u_3}{\partial x} + \dot{u}_3D_c\delta u_3\right)dydx \\ \delta W_{ext} = \int_0^L \int_{-b/2}^{+b/2} p_3\delta u_3\, dydx \\ \delta W_k = \int_0^L \left(\dot{u}_1I_0\delta\dot{u}_1 + \dot{u}_1I_1\delta\dot{\theta}_1 + \dot{\theta}_1I_1\delta\dot{u}_1 + \dot{\theta}_1I_2\delta\dot{\theta}_1 + \dot{u}_3I_0\delta\dot{u}_3\right)dx \end{cases} \tag{21}$$

With dot above a function signifies partial differentiation with respect to the time variable t. The inertia resultants I_0, I_1 and I_2 are defined as follows:

$$(I_0, I_1, I_2) = \int_{-b/2}^{b/2}\int_{-h/2}^{h/2}(\rho(z), z\rho(z), z^2\rho(z))dzdy \tag{22}$$

3. Solution Procedure Based on The FEM With The NITINM

In this section, the FEM [28,29] and the NITINM [30] are applied to solve the governing equations.

3.1. Spatial approximation using FEM

In this study, two-noded C^0 beam elements with a length of $l^{(e)}$ and three degrees of freedom per node are employed to discretize the kinematic variables. The axial displacement u_1, deflection u_3, and rotation θ_1 are interpolated using linear Lagrangian shape functions as follows:

$$\begin{cases} u_1(\xi) =< N_a(\xi) > \{d^{(e)}\} \\ u_3(\xi) =< N_d(\xi) > \{d^{(e)}\} \\ \theta_1(\xi) =< N_r(\xi) > \{d^{(e)}\} \end{cases} \quad (23)$$

Where $\{d^{(e)}\}$ represents the nodal displacement vector for the e th element, defined as:

$$\{d^{(e)}\} =< u_1^1, u_3^1, \theta_1^1, u_1^2, u_3^2, \theta_1^2 >^T \quad (24)$$

Where $u_1^1, u_3^1, \theta_1^1, u_1^2, u_3^2$, and θ_1^2 denote the axial displacement, deflection, and rotation at nodes 1 and 2 of the eth element, respectively. The vectors $\langle N_a \rangle, \langle N_d \rangle$ and $\langle N_r \rangle$ are row vectors consisting of C^0 shape functions, and are defined as follows:

$$\begin{cases} \langle N_a(\xi) \rangle = \langle N_1(\xi), 0, 0, N_2(\xi), 0, 0 \rangle \\ \langle N_d(\xi) \rangle = \langle 0, N_1(\xi), 0, 0, N_2(\xi), 0 \rangle \\ \langle N_r(\xi) \rangle = \langle 0, 0, N_1(\xi), 0, 0, N_2(\xi) \rangle \end{cases} \quad (25)$$

Where $N_1(\xi)$ and $N_2(\xi)$ are the standard linear shape functions, defined as:

$$\begin{cases} N_1(\xi) = (1-\xi)/2 \\ N_2(\xi) = (1+\xi)/2 \end{cases} \quad (26)$$

Where $\xi \in [-1,1]$ represents the natural coordinates, expressed as $\xi(x) = -1 + 2x/l^{(e)}$. By applying Eqs. (15) And (23), the generalized strains e_{11}, κ_{11} and χ_{13} can be expressed in terms of the nodal degrees of freedom as:

$$\begin{cases} e_{11}(\xi) =< B_m(\xi) > \{d^{(e)}\} \\ \kappa_{11}(\xi) =< B_b(\xi) > \{d^{(e)}\} \\ \chi_{13}(\xi) =< B_s(\xi) > \{d^{(e)}\} \end{cases} \quad (27)$$

Where the kinematic vectors $\langle B_m \rangle, \langle B_b \rangle$ and $\langle B_s \rangle$ are defined as:

$$\begin{cases} \langle B_m \rangle = \dfrac{d\xi}{dx}\left\langle \dfrac{dN_a}{d\xi} \right\rangle \\ \langle B_b \rangle = \dfrac{d\xi}{dx}\left\langle \dfrac{dN_r}{d\xi} \right\rangle \\ \langle B_s \rangle = \dfrac{d\xi}{dx}\left\langle \dfrac{dN_d}{d\xi} \right\rangle + \langle N_r \rangle \end{cases} \quad (28)$$

Where $\frac{d\xi}{dx} = 1/\det(J)$, with $\det(J)$ being the Jacobian, equal to $l^{(e)}/2$. By applying Eqs. (20), (21), (23), and (27), the discretized governing equation is derived as:

$$[M^g]\{\ddot{U}^g(t)\} + [C^g]\{\dot{U}^g(t)\} + [K^g]\{U^g(t)\} = \{F^g(t)\} \quad (29)$$

Here,$[M^g], [C^g], [K^g]$, and $\{F^g\}$ denote the global mass, damping, stiffness matrices, and external force vector, respectively, assembled as follows:

$$([M^g], [C^g], [K^g], \{F^g\}, \{U^g\}) = \sum_{e=1}^{e=N_{\text{elem}}} \left(\left[M^{(e)}\right], \left[C^{(e)}\right], \left[K^{(e)}\right], \left\{F^{(e)}\right\}, \left\{U^{(e)}\right\} \right) \quad (30)$$

With

$$\begin{cases}\left[K^{(e)}\right] = [K^{mme}] + [K^{bbe}] + [K^{sse}] + [K^{wfe}] + [K^{pfe}] \\ \left[M^{(e)}\right] = [M^{mme}] + [M^{bbe}] + [M^{sse}]\end{cases} \quad (31)$$

Where the element matrices are defined as:

$$\begin{cases}[K^{mme}] = \int_0^{l^{(e)}} \{B_m\}A < B_m > dx + \int_0^{l^{(e)}} \{B_m\}A < B_b > dx + \int_0^{l^{(e)}} \{B_b\}A < B_m > dx \\ [K^{bbe}] = \int_0^{l^{(e)}} \{B_b\}D < B_b > dx \\ [K^{sse}] = \int_0^{l^{(e)}} \{B_s\}C < B_s > dx \\ [K^{wfe}] = \int_0^{l^{(e)}} \{N_d\}bK_w < N_d > dx \\ [K^{pfe}] = \int_0^{l^{(e)}} \frac{d\xi}{dx}\left\{\frac{dN_d}{d\xi}\right\}bK_p\frac{d\xi}{dx} < \frac{dN_d}{d\xi} > dx \\ [M^{mme}] = \int_0^{l^{(e)}} \{N_a\}I_0 < N_a > dx + \int_0^{l^{(e)}} \{N_a\}I_1 < N_r > dx + \int_0^{l^{(e)}} \{N_r\}I_1 < N_a > dx \\ [M^{bbe}] = \int_0^{l^{(e)}} \{N_r\}I_2 < N_r > dx \\ [M^{sse}] = \int_0^{l^{(e)}} \{N_d\}I_0 < N_d > dx \\ \left[C^{(e)}\right] = \int_0^{l^{(e)}} \{N_d\}bC_D < N_d > dx \\ \left\{F^{(e)}\right\} = \int_0^{l^{(e)}} b\{N_d\}p_3 dx\end{cases} \quad (32)$$

The equation of motion (Eq. 29) is completed by the essential boundary conditions, which are given in the next section (Eqs. 38, 39, and 40).

3.2. Temporal Approximation Using The NITINM

In this study, the NITINM is employed to solve Eq. (29). This method allows the approximation of the velocity $\{\dot{U}^g(t+\Delta t)\}$ and acceleration $\{\ddot{U}^g(t+\Delta t)\}$ vectors at time $t+\Delta t$ as follows [30]:

$$\begin{cases}\{\ddot{U}^g(t+\Delta t)\} = a_0^N(\{U^g(t+\Delta t)\} - \{U^g(t)\}) - a_2^N\{\dot{U}^g(t)\} - a_3^N\{\ddot{U}^g(t)\} \\ \{\dot{U}^g(t+\Delta t)\} = \{\dot{U}^g(t)\} + a_6^N\{\ddot{U}^g(t)\} + a_7^N\{\ddot{U}^g(t+\Delta t)\}\end{cases} \quad (33)$$

Where Δt is the time step, the coefficients $a_0^N, a_1^N, a_2^N, a_3^N, a_4^N, a_5^N, a_6^N$, and a_7^N are defined as:

$$\begin{cases}a_0^N = 1/(\alpha^N\Delta t^2) \\ a_1^N = \delta^N/(\alpha^N\Delta t) \\ a_2^N = 1/(\alpha^N\Delta t) \\ a_3^N = 1/(2\alpha^N) - 1 \\ a_4^N = \delta^N/\alpha^N - 1 \\ a_5^N = (\Delta t/2)(\delta^N/\alpha - 2) \\ a_6^N = \Delta t(1-\delta^N) \\ a_7^N = \delta^N\Delta t\end{cases} \quad (34)$$

Where δ^N and α^N are the Newmark parameters, selected as 0.5 and 0.25, respectively. Applying Eq. (33), the resulting algebraic equations are:

$$\left\{\left[\hat{K}^g\right]_{t+\Delta t}\{U^g(t+\Delta)\} = \{\hat{F}\}_{t,t+\Delta t}\right. \tag{35}$$

Where $\{U^g(t+\Delta)\}$ represents the global generalized displacement at time $t+\Delta$. The effective stiffness matrix $\left[\hat{K}^g\right]_{t+\Delta t}$ and the load vector $\{\hat{F}\}_{t,t+\Delta t}$ at time $t+\Delta t$ are defined as:

$$\begin{cases} \left[\hat{K}^g\right]_{t+\Delta t} = [K^g]_{t+\Delta t} + a_0^N[M^g]_{t+\Delta t} + a_1^N[C^g]_{t+\Delta t} \\ \{\hat{F}\}_{t,t+\Delta t} = \{F\}_{t+\Delta t} + [M^g]_{t+\Delta t}(a_0^N\{U^g(t)\} + a_2^N\{\dot{U}^g(t)\} + a_3^N\{\ddot{U}^g(t)\}) \\ \qquad\qquad +[C^g]_{t+\Delta t}(a_1^N\{U^g(t)\} + a_4^N\{\dot{U}^g(t)\} + a_5^N\{\ddot{U}^g(t)\}) \end{cases} \tag{36}$$

The acceleration vector $\{\ddot{U}^g(0)\}$ is determined at $t=0$ as follows:

$$\{\ddot{U}^g(0)\} = \left[\hat{M}^g\right]^{-1}\left(\{\hat{F}\}_0 - \left[\hat{C}^g\right]\{\dot{U}^g(0)\} - \left[\hat{K}^g\right]\{U^g(0)\}\right) \tag{37}$$

4. Results and Discussion

This section examines the linear forced vibration characteristics of polymer matrix composite beams (PMCBs) reinforced with hybrid functionally graded boron nitride nanotubes and carbon fiber (FG-BNNT/CF). The FG-BNNT/CF reinforced PMCBs are subjected to a vertical sudden dynamic load and analyzed under two types of boundary conditions, supported by viscoelastic foundations as shown in Figure 1. Four different BNNT distribution patterns are considered, with carbon fiber uniformly distributed. The study investigates how the BNNT weight fraction, BNNT distribution patterns, carbon fiber volume fraction, elastic foundation stiffness, and boundary conditions affect the dynamic behavior of FG-BNNT/CF reinforced PMCBs.

4.1. Preliminary Remarks

Unless stated otherwise, the geometric properties of the PMCBs are provided in Table 3.

Table 3. Geometric characteristics of the PMCBs

Parameter	Values
$L(m)$	1
$b(m)$	1
$h(m)$	0.01

The analysis considers only a sudden vertical dynamic load, $p_3(x,t) = 1$ N/m, as indicated in

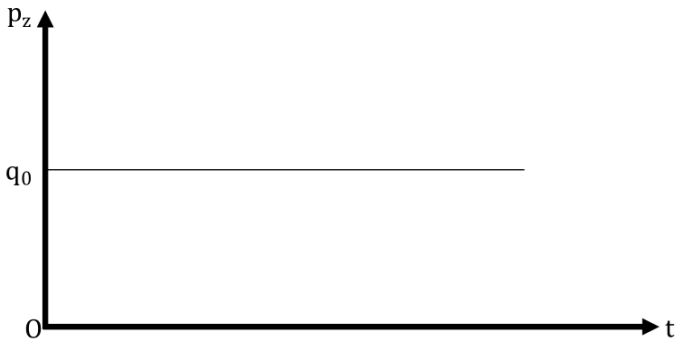

Fig. 3. The sudden transverse dynamic load applied to the FG-BNNT/CF reinforced polymer matrix composite beams

Three types of boundary conditions, which are clamped-clamped (C-C), simply supported-simply supported (S-S), and clamped-free (C-F) are considered in this paper:

$$(C-C):\begin{cases}u_1=u_3=\theta_1=0 \text{ at } x=0\\ u_1=u_3=\theta_1=0 \text{ at } x=L\end{cases} \tag{38}$$

$$(S-S):\begin{cases}u_1=u_3=0 \text{ at } x=0\\ u_1=u_3=0 \text{ at } x=L\end{cases} \tag{39}$$

$$(C-F): u_1=u_3=\theta_1=0 \text{ at } x=0 \tag{40}$$

4.2. Numerical Convergence and Comparative Validation

To evaluate the accuracy and validity of the current numerical model using FEM with NITINM based FSDT, convergence studies were first performed on a C-C elastic homogeneous isotropic beam. The beam's geometric and material specifications are specified as follows [27]:

$$L_1=1 \text{ m} \quad ; \quad L_2=1 \text{ m} \quad ; h=0.01 \text{ m} \tag{41}$$

The external force vector is assumed to be null, and the beam is initialized with the following conditions:

$$\begin{cases}u_3(x,0) &= \sin(\pi x)-\pi x(1-x) & \text{for } x\in[0,L]\\ \dot{u}_3(x,0) &= 0 & \text{for } x\in[0,L]\\ \theta_1(x,0) &= -\pi\cos(\pi x)+\pi(1-2x) & \text{for } x\in[0,L]\\ \dot{\theta}_1(x,0) &= 0 & \text{for } x\in[0,L]\end{cases} \tag{42}$$

The Newmark integration parameters are chosen as $\delta^N=1/2, \alpha^N=1/4$, with a time increment of $\Delta t=0.005s$. Figure 4 illustrates the time history of the transverse displacement at the beam's mid-span for various element discretizations N_{elem}.

Figure 4 indicates that the optimal number of elements is 100. Consequently, this value will be utilized for the subsequent numerical analyses. The comparison in Table 6 highlights the accuracy of the proposed method against reference FEM solutions based on Euler-Bernoulli beam theory (EBT) and Timoshenko beam theory (TBT). The displacement histories obtained from the present approach exhibit almost perfect agreement with both reference models. The maximum deviation with respect to FEM (EBT) is less than 0.2%, while the deviation with respect to FEM (TBT) remains below 1.3% throughout the entire time interval. Such small errors confirm that the present formulation can reliably capture the dynamic response of beams, while maintaining computational efficiency. These results provide strong validation of the proposed methodology and demonstrate its consistency with established finite element solutions.

Figure 5 demonstrates the time-step sensitivity of the Newmark integration scheme for the central deflection of the homogeneous isotropic beam. The results for $\Delta t=0.005$ s and finer ($\Delta t=0.0005$ and 0.00005 s) are indistinguishable, while $\Delta t=0.01$ s introduces only a negligible deviation in amplitude. This confirms that $\Delta t=0.005$ s is adequate for the homogeneous validation cases. For the composite parametric study, a smaller increment $\Delta t=0.0005$ s was adopted to safely capture the higher-frequency response. For the first validation study, we consider the free vibration response of functionally graded beams with the following geometric and material parameters:

$$L=3.52\times10^{-4}m \text{ ; } b=3.52\times10^{-5}m \text{ ; } h=17.6\times10^{-6} \text{ m}$$

$$E_1=14.4 \text{ GPa ; } E_2=1.44 \text{ GPa ; } \nu=0.38 \text{ ; } K_s=\frac{5(1+\nu)}{6+5\nu} \tag{43}$$

$$\rho_1=1.22\times10^{4}kg/m \text{ ; } \rho_2=1.22\times10^{3}\ kg/m$$

The rotary inertia is included in the present study. Table 5 contains the results for homogeneous ($n=0$) and functionally graded ($n\neq0$) compared to the same given by Reddy [27].

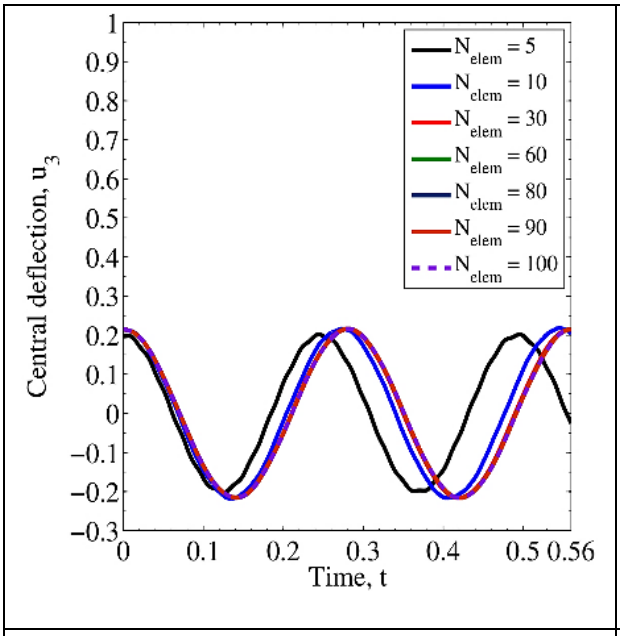

Fig. 4. Central transverse displacement $u_3(0.5,t)$ versus time t with different numbers of elements N_{elem} for a C-C isotropic homogeneous elastic beam

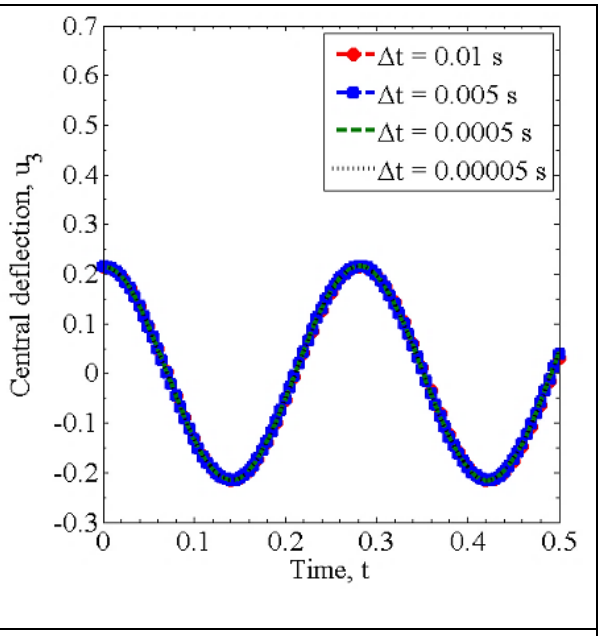

Fig. 5. Central transverse displacement $u_3(0.5,t)$ versus time t with different time steps Δt for a C-C isotropic homogeneous elastic beam

Table 4. Quantitative validation of the present method through comparison with FEM (EBT and TBT) solutions, including relative percentage errors

Time	Method				
	$u_3(Present)$	$u_3(EBT)$	$u_3(TBT)$	Err vs EBT (%)	Err vs TBT (%)
0	2.1460	2.146	2.146	0.000	0.000
0.01	2.0974	2.098	2.100	0.029	0.124
0.02	1.9504	1.951	1.953	0.031	0.133
0.03	1.6978	1.698	1.695	0.012	0.165
0.04	1.3501	1.350	1.342	0.007	0.604
0.05	0.9363	0.935	0.929	0.139	0.786
0.06	0.4844	0.483	0.484	0.290	0.083
0.07	0.0184	0.018	0.016	2.222	15.000
0.08	−0.4536	−0.455	−0.469	0.308	3.284
0.09	−0.9140	−0.916	−0.937	0.218	2.455
0.10	−1.3330	−1.336	−1.349	0.225	1.186
0.11	−1.6799	−1.682	−1.680	0.125	0.006
0.12	−1.9307	−1.932	−1.931	0.067	0.016
0.13	−2.0864	−2.087	−2.100	0.029	0.648
0.14	−2.1478	−2.148	−2.168	0.009	0.932
0.15	−2.1105	−2.111	−2.116	0.024	0.260

Table 5. First three natural frequencies $\left(\bar{\omega}_n = \omega_n L^2/\sqrt{\rho_2 A_0/E_2}\right)$ of simply-supported FGM beams

n	$\bar{\omega}_1$		$\bar{\omega}_2$		$\bar{\omega}_3$	
	ref [27]	Present	ref [27]	Present	ref [27]	Present
0	9.83	9.8353	38.82	38.9412	85.63	86.2024
1	8.67	8.6730	34.29	34.3826	75.79	76.0537
10	10.28	10.2898	40.47	40.5756	88.80	88.2976

A close agreement between the two solutions demonstrates the accuracy and reliability of the present approach. For the second validation study, we consider an isotropic, homogeneous elastic beam with the following initial conditions:

$$\begin{cases} u_3(x,0) = \cosh(\lambda x) - \cos(\lambda x) - (\cos(\lambda L) + \cosh(\lambda L))/(\sin(\lambda L) & \text{for } x \in [0,L] \\ \quad + \sinh(\lambda L))(\sinh(\lambda x) - \sin(\lambda x)) & \\ \theta_1(x,0) = \lambda(\sinh(\lambda x) + \sin(\lambda x)) - (\cos(\lambda L) + \cosh(\lambda L))/(\sin(\lambda L) & \text{for } x \in [0,L] \\ \quad + \sinh(\lambda L))(\cosh(\lambda x) - \cos(\lambda x))\lambda & \end{cases} \tag{44}$$

Where $\lambda = 1.8751/L$. The geometric and material parameters are provided in Eq. (41). The analytical solution is given as:

$$u_3(x,t) = (\cosh(\lambda x) - \cos(\lambda x) - (\cos(\lambda L) + \cosh(\lambda L))/(\sin(\lambda L) + \sinh(\lambda L))(\sinh(\lambda x) - \sin(\lambda x)))\cos(\omega t) \tag{45}$$

In which $\omega = \lambda^2\sqrt{(EI/\rho A)}$. Fig. 6 presents graphs of the central transverse displacement $u_3(0.5L,t)$ versus time t for both the current FEM-based numerical model and the exact solution (Eq. (44)).

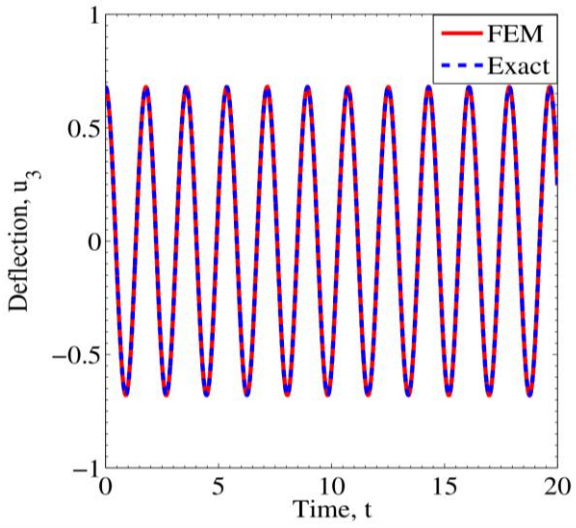

Fig. 6. Central transverse displacement $u_3(0.5L,t)$ versus time t obtained by FEM and compared to the exact solution

Figure 6 demonstrates that our results closely align with the exact solution, confirming the accuracy and reliability of the current numerical model. In the final verification numerical experiment, a straight, thick ($L = 2m, b = 0.2$ m, $h = 0.6$ m) elastic homogeneous isotropic beam was investigated where both rotary inertia and known shear deformation effects were considered. The beam's left boundary is fixed (i.e., $u_x = u_z = \theta_x = 0$ at $= 0$), free at the right end ($x = L_1$), and subjected to a uniformly distributed sudden dynamic transverse load of intensity $p_0 =$ 100kN/m. The material properties of the beam are: $= 50$GPa, $v = 0.2, \rho = 2500$ kg/m^3, and since the FSDT is adopted, a shear correction factor of 5/6 is applied. The initial conditions are taken as zero displacement and zero velocity vectors. For the numerical analyses, the following parameters are employed: $N_{\text{elem}} = 100$, the total duration of the simulation is $T = 0.05s$, the temporal step size is $\Delta t = 10^{-6}s$, with $\delta^N = 1/2$ and $\alpha^N = 1/4$. Figure 6 shows a comparison of the tip vertical displacement $u_3(L_1,t)$ as a function of time t, obtained using Abaqus and the proposed numerical approach.

It is evident from Fig. 7 that the obtained results exhibit excellent agreement with those derived from the Abaqus software. Based on the presented numerical experiments, it can be concluded that the proposed approach accurately simulates the linear dynamic response of thick elastic beams. To assess the accuracy and consistency of the adopted micromechanical modeling approaches, a comparative analysis is conducted between the Rule of Mixtures (ROM) and Mori–Tanaka (MT) homogenization schemes. Table 6. Comparison of Root Mean Square Errors (RMSE) between the

adopted micromechanical model and the Mori–Tanaka (MT) homogenization approach under C–C boundary conditions, considering various distribution patterns, carbon fiber volume fractions, and BNNT weight fractions.

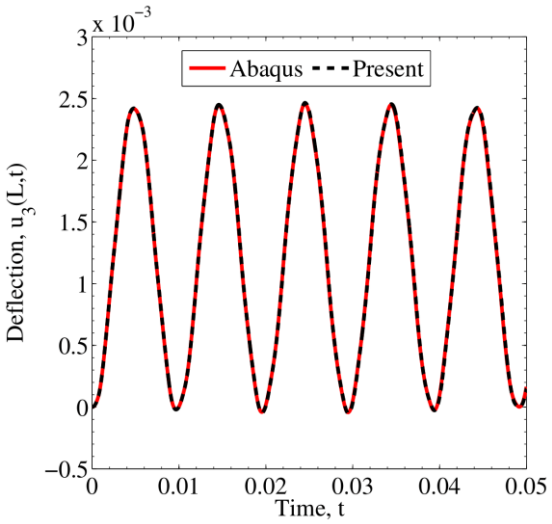

Fig. 7. Tip transverse displacement $u_3(L,t)$ versus time t obtained by FEM and compared to the Abaqus solution

Table 6. Comparison of the Root Mean Square Error (RMSE) between the Rule of Mixtures (ROM) and Mori-Tanaka (MT) homogenization approaches

Distribution patterns	V_{CF}	W_{rGO}	RMSE
UD	0.01	0.5%	7.3241×10^{-9}
		1%	5.7537×10^{-9}
		2%	3.4636×10^{-9}
	0.03	0.5%	1.9260×10^{-8}
		1%	1.6820×10^{-8}
		2%	1.2020×10^{-8}
FG-X	0.01	0.5%	6.3670×10^{-9}
		1%	4.2712×10^{-9}
		2%	1.5103×10^{-9}
	0.03	0.5%	1.7238×10^{-8}
		1%	1.3566×10^{-8}
		2%	7.1389×10^{-9}
FG-O	0.01	0.5%	8.2724×10^{-9}
		1%	7.5901×10^{-9}
		2%	6.0033×10^{-9}
	0.03	0.5%	2.1208×10^{-8}
		1%	2.0429×10^{-8}
		2%	1.8197×10^{-8}
FG-V	0.01	0.5%	7.4346×10^{-9}
		1%	6.0719×10^{-9}
		2%	4.0710×10^{-9}
	0.03	0.5%	1.9400×10^{-8}
		1%	1.7231×10^{-8}
		2%	1.2995×10^{-8}

Table 6 presents a comparison of the Root Mean Square Error (RMSE) between the Rule of Mixtures (ROM) and Mori-Tanaka (MT) homogenization approaches for the case of C-C beam with different distribution patterns (UD, FG-X, FG-O, FG-V), carbon fiber volume fractions (V_{CF}), and BNNT

weight fractions (W_{BNNT}). The RMSE values are consistently very low across all cases, generally in the order of 10^{-9} to 10^{-8}, indicating excellent agreement between the two homogenization methods. These results confirm that both, the adopted micromechanical model and MT homogenization approaches yield highly consistent dynamic responses for nanocomposite beams, with differences that are negligible for engineering purposes. The choice of homogenization method can be guided by convenience and computational cost, particularly in cases with complex distribution patterns or high fiber contents.

4.3. Parametric Analysis

In this subsection, we present results to investigate the impact of various geometric and material parameters on the linear forced vibration response of FG-BNNT/CF reinforced polymer matrix composite beams. The geometric and material properties of the considered PMCBs are provided in Table 1. For the numerical analyses, the following parameters are used: the number of elements $N_{\text{elem}} = 100$, the total simulation time $T = 0.5$ s, the time step $\Delta t = 0.0005s$, with $\delta^N = 1/2$ and $\alpha^N = 1/4$. Additionally, both the initial displacement and velocity vectors are assumed to be zero. In all the parametric studies conducted, C-C (Eq. (38)), S-S ((Eq. (39))), and C-F (Eq. (40)) boundary conditions are considered.

4.3.1. Influence of BNNT Weight Fraction

In this study, the influence of the BNNT weight fraction (W_{BNNT}) on the dynamic behavior of FG-BNNT/CF reinforced PMCBs without VEFs ($K_w = K_p = C_D = 0$) is evaluated. Different values of BNNT weight-fractions (0%, 0.5%, 1%, and 2%) with a UD BNNT distribution are considered. The CF volume fraction is taken as $V_{CF} = 0.01$. Figs. 8(a), 8(b), and 8(c) present the central vertical displacements of C-C, S-S, and C-F FG-BNNT/CF reinforced PMCBs subjected to a vertical dynamic step load.

Figures 8(a), 8(b), and 8(c) show that increasing the BNNT/CF weight fraction W_{BNNT} affects the amplitude and period of the central vertical displacement in FG-BNNT/CF reinforced PMCBs because higher reinforcement content enhances the stiffness and mass distribution of the beam, increasing its resistance to bending and altering its natural frequency. Specifically, higher BNNT/CF weight fractions lead to a reduction in both amplitude and period, since the stiffer material reduces dynamic deflections and accelerates the vibrational response, effectively shortening the oscillation period. This effect is significant under both boundary conditions. Additionally, the maximum amplitude and period of the central vertical displacement are observed under S-S boundary conditions, compared to C-C BCs because simply-supported beams are less constrained, allowing larger deflections and longer vibration periods, with the C-F beam consistently showing higher amplitudes and temporal periods compared to both C-C and S-S cases as the cantilever-free configuration is inherently more flexible, amplifying the impact of dynamic loads on both displacement magnitude and oscillation duration.

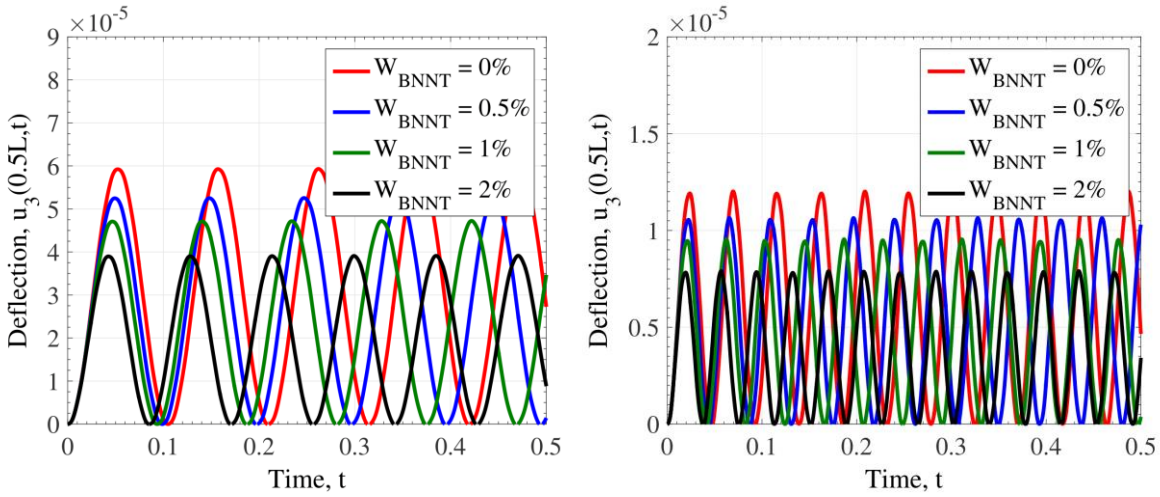

(a) C-C FG-BNNT/CF reinforced PMCBs

(b) S-S FG-BNNT/CF reinforced PMCBs

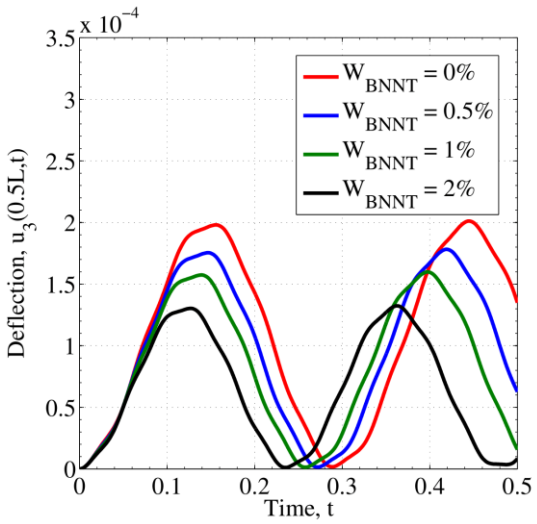

(c) C-F FG-BNNT/CF reinforced PMCBs

Fig. 8. Central transverse displacement $u_3(0.5L, t)$ versus time t for FG-BNNT/CF reinforced PMCBs with varying BNNT weight fractions under C-C (8(a)), S-S (8(b)) and C-F (8(c)) boundary conditions

4.3.2. Influence of BNNT Distribution Patterns

To investigate the impact of BNNT distribution patterns on the time-history curve of central vertical displacement in FG-BNNT/CF reinforced PMCBs without a viscoelastic foundation, four BNNT distribution patterns (UD, FG-X, FG-O, and FG-V) are analyzed. The CF volume fraction is set at $V_{CF} = 0.01$ and the BNNT weight fraction is chosen as $W_{BNNT} = 1\%$. Figures 9(a), 9(b), and 9(c) present the time-history curves of central vertical displacement for UD and three types of FG-BNNT reinforced PMCBs under a vertical dynamic step load, with C-C, S-S, and C-F boundary conditions, respectively. As shown in Figs. 9(a), 9(b), and 9(c) for both C-C, C-F, and S-S BCs, the FG-O-BNNT reinforced PMCBs exhibits the highest amplitude and period of central vertical displacement, whereas the FG-X-BNNT configuration shows the lowest values because the O-type distribution concentrates the stiff BNNTs near the surfaces, increasing the bending rigidity and natural frequency, while the X-type distribution spreads the reinforcement more uniformly, reducing the beam's ability to resist transverse deformation.

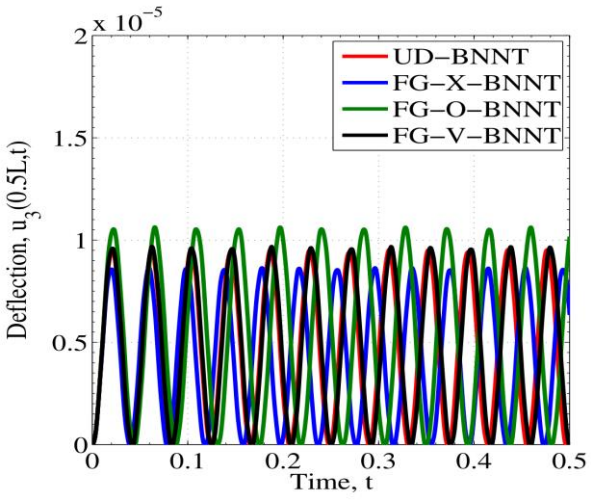

(a) C-C FG-BNNT/CF reinforced PMCBs

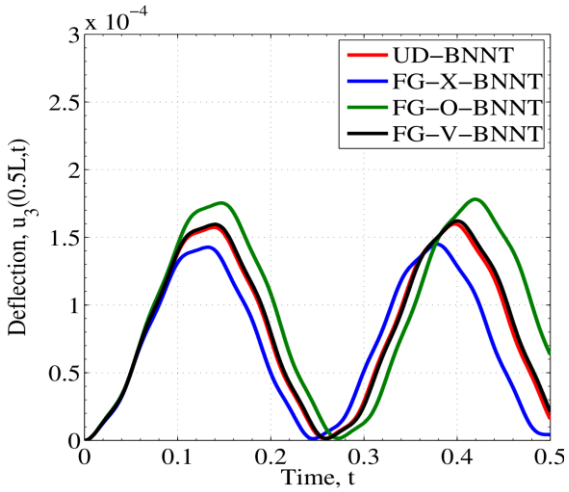

(b) C-F FG-BNNT/CF reinforced PMCBs

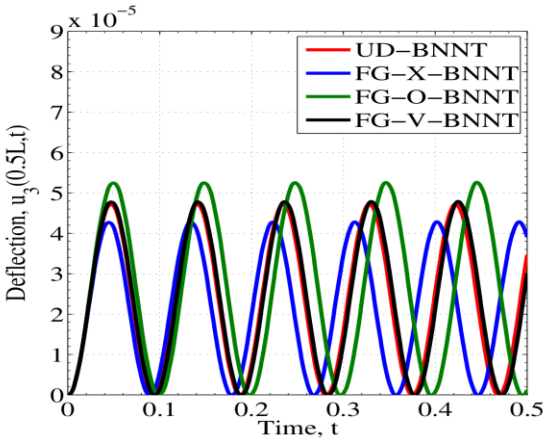

(c) S-S FG-BNNT/CF reinforced PMCBs

Fig. 9. Central transverse displacement $u_3(0.5L, t)$over time t for FG-BNNT/CF reinforced PMCBs with different BNNT distribution patterns under DL with C-F (9(a)), S-S(9(b)) and S-S (9(c)) boundary conditions

Therefore, it can be concluded that distributing BNNT near the top and bottom surfaces of the FG-BNNT reinforced PMCBs is the optimal choice for enhancing the global rigidity of the PMCBs since this placement maximizes the moment of inertia and improves the beam's resistance to bending under dynamic loads, effectively reducing vibration amplitude and period. The influence of the BNNT distribution patterns on the dynamic response is more significant for the C-F beams compared to the S-S and C-C cases because the initially flexible C-F beams experience larger dynamic deflections, making the effect of reinforcement heterogeneity more pronounced on their vibration characteristics. This is attributed to the enhanced flexibility of the C-F configuration, which amplifies the impact of material heterogeneity on the vibration characteristics.

4.3.3. Influence of BNNT Geometrical Parameters

To investigate the influence of BNNT geometrical parameters on the central vertical displacement of PMCBs reinforced with FG-BNNTs, the FG-X distribution model is adopted. The mass fraction of BNNTs is fixed at $W_{BNNT} = 1\%$, while the volume fraction of carbon fibers is set to $V_{CF} = 0.03$. The viscoelastic foundation parameters, namely K_w(N/m^2), K_p(N/m), and D_c(N $\cdot$ s/m^2), are assumed to be zero. Four aspect ratios, namely $100, 200, 300$, and 400, are considered. The time-history curves of the central vertical displacement of FG-X-BNNT reinforced PMCBs, subjected to a step-type vertical dynamic load, are presented in Figures 10(a),10(b), and 10(c) for the $C-C, S-S$, and $C-F$ boundary conditions, respectively.

The effect of the aspect ratio is clearly observed in the dynamic response of FG-BNNT reinforced PMCBs. As the aspect ratio increases from 100 to 400, both the amplitude and the oscillation period of the central vertical displacement decrease significantly, reflecting the higher global stiffness of slender beams. This trend is consistent across all boundary conditions, although the reduction is more pronounced for the C–F case due to its greater flexibility. Consequently, higher aspect ratios contribute to improved structural rigidity and vibration resistance, highlighting the crucial role of geometric parameters in optimizing the dynamic performance of FG-BNNT reinforced PMCBs.

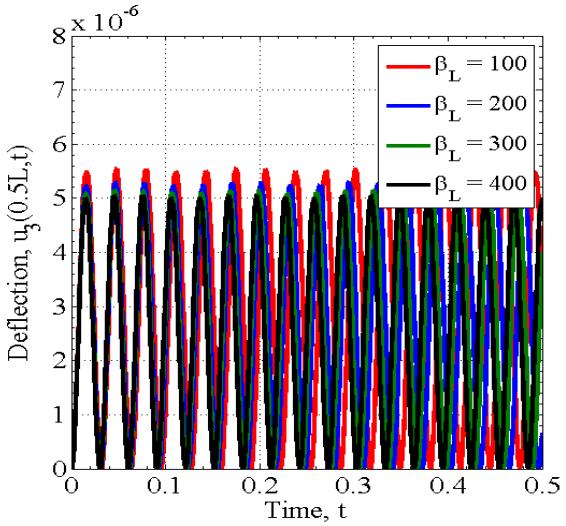

(a) C-C FG-BNNT/CF reinforced PMCBs

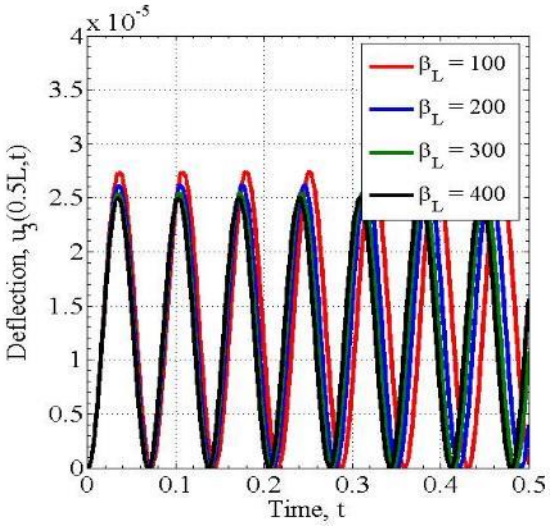

(b) C-F FG-BNNT/CF reinforced PMCBs

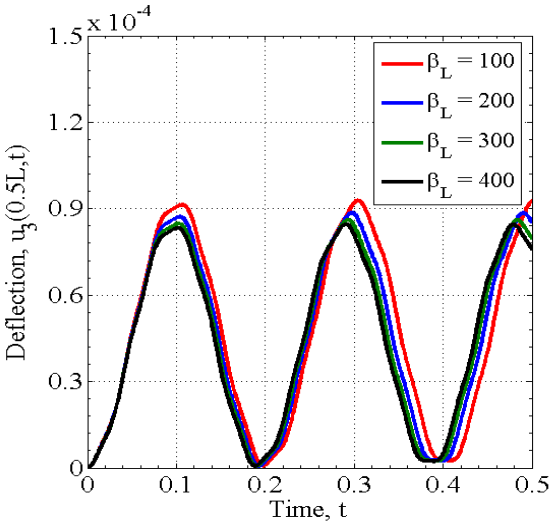

(c) S-S FG-BNNT/CF reinforced PMCBs

Fig. 10. Time-history curves of the central transverse displacement $u_3(0.5L, t)$ of FG-BNNT/CF reinforced PMCBs with different BNNT aspect ratios under dynamic loading for (a) C–F, (b) S–S, and (c) C–C boundary conditions

4.3.3. Influence of Viscoelastic Damping Coefficient

To examine the effect of the viscoelastic damping coefficient on the central vertical displacement of FG-BNNT reinforced PMCBs, the FG-X distribution pattern is used. The BNNT weight fraction is set at $W_{BNNT} = 1\%$ with a CF volume fraction of $V_{CF} = 0.01$. The viscoelastic foundation parameters $K_w(N/m^2)$ and $K_p(N/m)$ are assumed to be zero, while the damping coefficient $D_c(\text{N.s/m}^2)$ varies from 0 to 5×10^2. The time-history curves of central vertical displacement for FG-X-BNNT reinforced PMCBs under a vertical dynamic step load are depicted in Figures 11(a), 11(b), and 11(c) for C-C, S-S, and C-F BCs, respectively.

Figs. 11(a), 11(b), and 11(c) illustrate that the damping parameter significantly affects the dynamic response of FGBNNT/CF reinforced PMCBs because damping dissipates vibrational energy, reducing the system's kinetic energy and limiting the amplitude of oscillations. As the damping coefficient increases, the amplitude of central vertical displacement decreases exponentially since higher damping removes energy from the system more efficiently, shortening the duration and intensity of vibrations under dynamic loads.

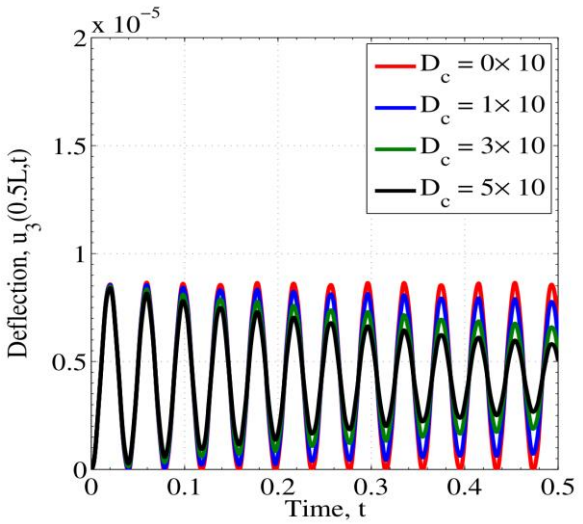

(a) C-C FG-BNNT/CF reinforced PMCBs

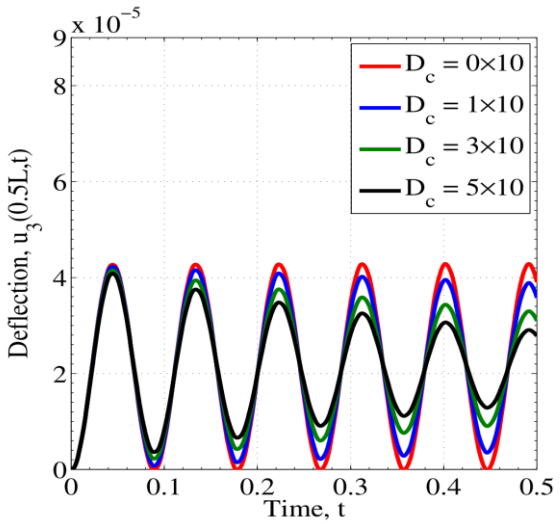

(b) S-S FG-BNNT/CF reinforced PMCBs

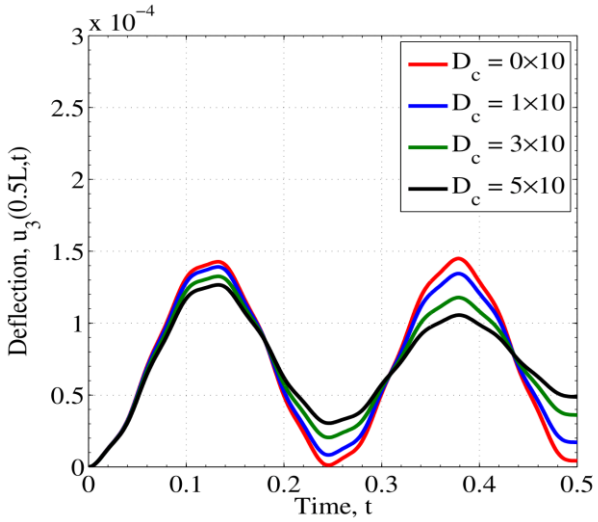

(c) C-F FG-BNNT/CF reinforced PMCBs

Fig. 11. Central transverse displacement $u_3(0.5L, t)$ over time t for FG-BNNT reinforced PMCBs with different viscoelastic damping coefficients D_c under DL with C-C (9(a)), S-S (11(b)) and C-F (11(c)) boundary conditions

The damping effect is particularly prominent in the C-F configuration, where the initial high flexibility allows for greater energy dissipation compared to the more constrained $C-C$ and $S-S$ beams because flexible beams experience larger oscillations, which generate more strain energy that can be absorbed by the damping mechanism, leading to a stronger reduction in vibration amplitude.

4.3.4. Influence of Winkler and Shear Viscoelastic Foundation Parameters

The effects of Winkler and shear layer stiffness on the dynamic behavior of thin FG-BNNT/CF reinforced PMCBs with C-C and S-S boundary conditions under a transverse load of 1 N/m on a viscoelastic foundation are investigated. The BNNT weight fraction is set at $W_{BNNT} = 1\%$ with a CF volume fraction of $V_{CF} = 0.01$ and a damping coefficient of $D_c = 10\ \mathrm{N.s/m^3}$. We examine three values for the Winkler foundation stiffness $K_w = (0{,}1 \times 10^4, 5 \times 10^4)$ and the shear layer parameter $K_p = (0{,}1 \times 10^3, 5 \times 10^3)$. Figs. 12(a), 12(b), and 12(c) present the central transverse displacement versus time for various values of the elastic foundation coefficients.

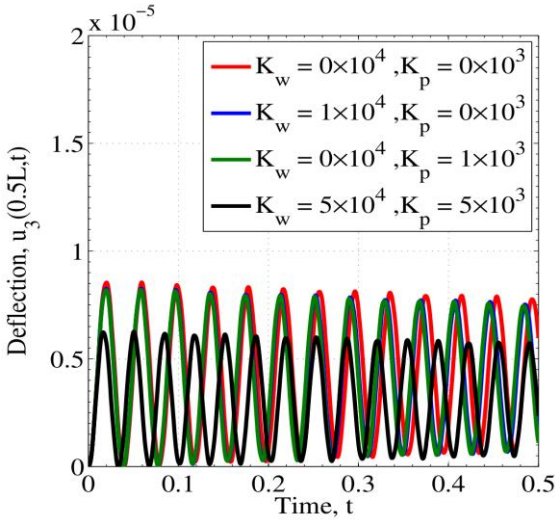

(a) C-C FG-BNNT/CF reinforced PMCBs

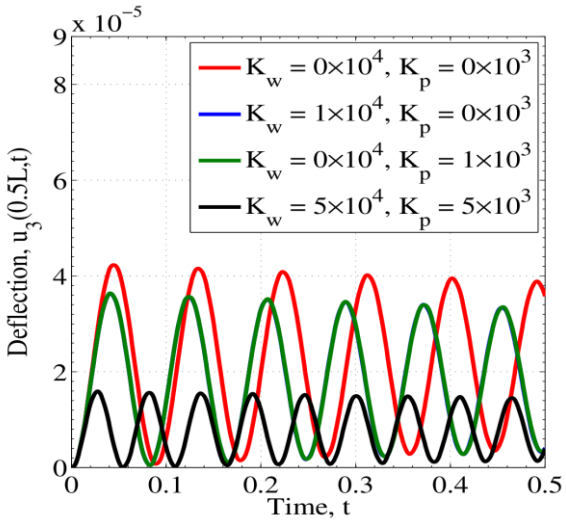

(b) S-S FG-BNNT/CF reinforced PMCBs

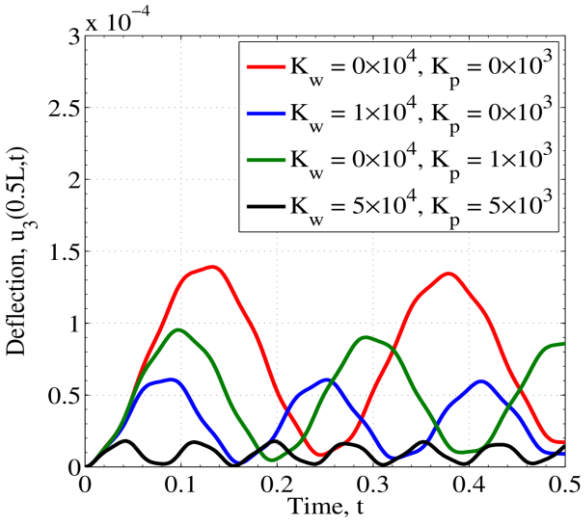

(c) C-F FG-BNNT/CF reinforced PMCBs

Fig. 12. Central transverse displacement $u_3(0.5L, t)$ versus time t for FG-BNNT reinforced PMCBs with different viscoelastic coefficients (K_W and K_p) under DL with C-C (12(a)), S-S (12(b)) and C-F (12(c)) boundary conditions

From Figs. 12(a), 12(b), and 12(c) it is observed that, as anticipated, that the central transverse displacement of the FG-BNNT/CF reinforced PMCBs decreases with increasing elastic foundation coefficients because a stiffer foundation provides higher reactive forces that counteract the dynamic bending of the beam, effectively increasing the system's overall dynamic stiffness. This outcome aligns with expectations because higher elastic foundation stiffness typically results in greater resistance to deformation, thereby reducing the amplitude of transverse displacement under the applied load as the beam's natural vibration is constrained by the foundation, leading to lower vibration amplitudes and modified dynamic response. The increase in Winkler and Pasternak foundation stiffness coefficients significantly suppresses the vibration amplitudes across all boundary conditions since the Winkler component resists local deflections while the Pasternak shear layer distributes the dynamic load more evenly, damping out oscillations. The C-F beams exhibit the most noticeable decrease in amplitude, reflecting their greater sensitivity to the elastic foundation parameters compared to the more rigid C − C and S − S beams because initially flexible beams experience larger dynamic displacements, so any increase in foundation stiffness has a proportionally stronger effect on their vibration suppression.

4.3.5. Influence of CF Volume Fraction

To assess the impact of CF volume fraction V_{CF} on the central vertical displacement of FG-BNNT/CF reinforced PMCBs, we consider C-C and S-S BCs with a UD transverse step load of 1 N/m applied to PMCBs resting on VEF ($K_w = 5 \times 10^4, K_p = 5 \times 10^3$, and $D_c = 10$). The BNNT weight fraction is set at $W_{BNNT} = 1\%$ with an FGX distribution pattern. Figures 13(a), 13(b), and 13(c) display the central transverse displacement versus time for various CF volume fractions.

From Figs. 13(a), 13(b), and 13(c) it is observed that as the CF volume fraction increases, the stiffness and strength of the PMCBs increase due to the enhanced load-bearing capacity of the CF, which improves the overall structural rigidity and resistance to deformation. This leads to a reduction in the amplitude of transverse displacement under given DMLs and BCs because the stiffer material can better resist bending and shear effects induced by dynamic loads. Conversely, a lower CF volume fraction results in a less stiff composite material. This lower stiffness means the beam is more flexible, leading to a larger amplitude of transverse displacement under the same loading conditions as the material offers less resistance to bending, allowing greater deflection under applied loads. However, the reduction is more substantial for the C-F beams due to their inherently lower stiffness, making them more sensitive to material reinforcement.

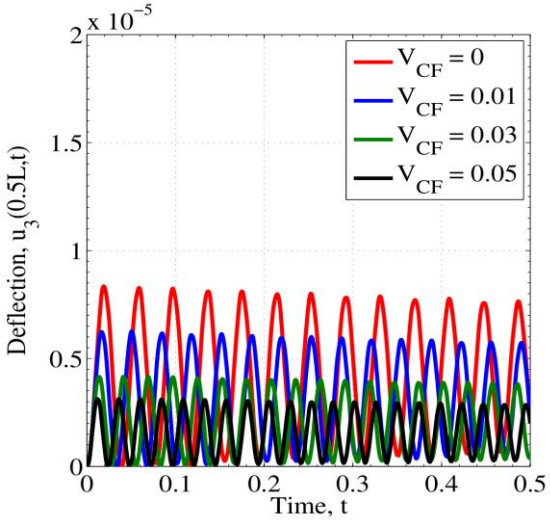

(a) C-C FG-BNNT/CF reinforced PMCBs

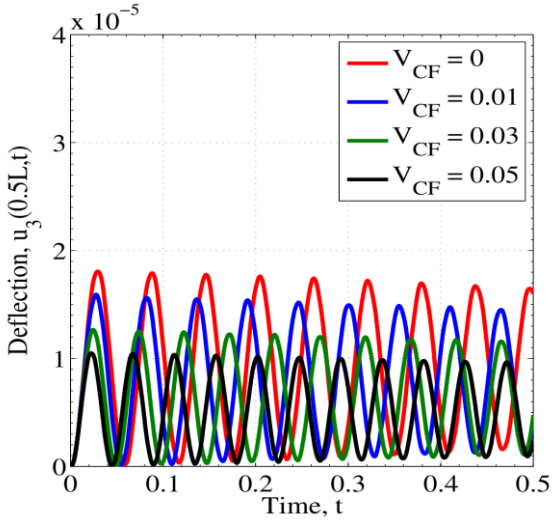

(b) S-S FG-BNNT/CF reinforced PMCBs

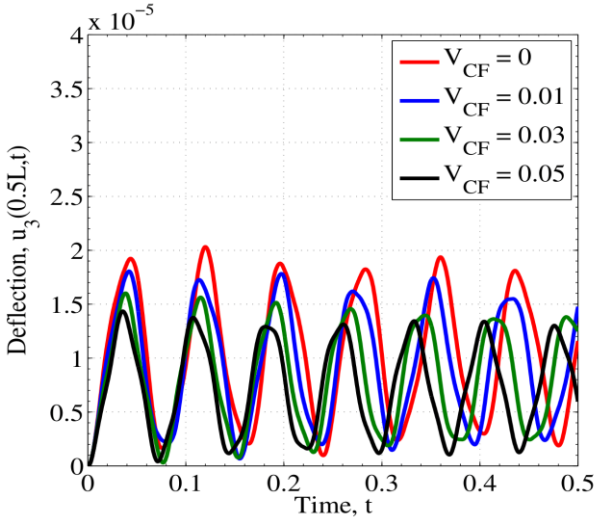

(c) C-F FG-BNNT/CF reinforced PMCBs

Fig. 13. Central transverse displacement $u_3(0.5L, t)$ as a function of time t for C-C (13(a)), S-S (13(b))and C-F (13(c)) boundary conditions, for different values of CF volume fraction

5. Conclusion

A detailed analysis was presented in this paper of the linear forced vibration analysis behavior of polymer matrix composite structural beams strengthened with an assembly of functionally graded boron nitride nanotubes and car bon fibers, supported by viscoelastic foundations under dynamic loads. Through the use of the Visco-Winkler-Pasternak model, this work captures the complex interactions between the composite beams and their surrounding environments, accounting for shear layer deformation, compressive stiffness, and damping effects. The beam's vibration behavior under various boundary conditions, loadings, and material configurations is examined using a first-order shear deformation structural beam model, the FEM, and Newmark technique. The results provide valuable insights into the dynamic characteristics of advanced composite structures, highlighting the potential of FG-BNNT/CF reinforcements to enhance mechanical performance and vibration control. The results provide a deeper understanding of the vibration characteristics of advanced composite structures, with particular focus on the control of vibrations in dynamic environments. The combination of FG-BNNT and CF reinforcements offers promising possibilities for enhancing the mechanical performance of composite beams, particularly in applications where maintaining structural integrity and controlling vibrations are essential for operational safety and longevity. These findings are particularly relevant for applications such as aerospace components, marine structures, and high-speed transportation systems, where lightweight materials with superior damping properties are essential for durability, safety, and comfort. Particularly, the findings can be used in concrete engineering problems such as the design of aerospace components, marine structures, and high-speed transportation systems, where lightweight materials with superior vibration damping characteristics are crucial for ensuring structural durability, passenger comfort, and operational safety. Moreover, the study lays the groundwork for future research on intelligent vibration control strategies, including adaptive and neural network-based approaches, to further optimize vibration reduction in complex dynamic environments and expand practical engineering applications. Further research could delve into the use of intelligent control strategies, including adaptive techniques and neural network-based controls, to optimize vibration reduction in more complex dynamic environments, broadening the scope for practical implementations in engineering systems.

Nomenclature

Table 7. List of Nomenclatures

L	Length of the composite beam	α_L	Longitudinal reinforcement efficiency factor of the Halpin–Tsai model
b	width of the composite beam	α_T	Transverse reinforcement efficiency factor of the Halpin–Tsai model
h	thickness of the composite beam	ξ_L	Longitudinal geometry parameter of the Halpin–Tsai model
S	cross-sections of the composite beam	ξ_T	Transverse geometry parameter of the Halpin–Tsai model
x, y, z	Cartesian coordinates along the beam	η_L	Longitudinal efficiency factor of the Halpin–Tsai model
x	Longitudinal coordinate along the length of the composite beam	η_T	Transverse efficiency factor of the Halpin–Tsai model
y	Transverse coordinate of the composite beam	$\rho_{BNNT/PM}$	mass density of the FG-BNNT reinforced PM
z	Vertical coordinate of the composite beam	ρ_{BNT}	mass densities of the BNNT
U_1	global displacements of the beam in the x-direction	ρ_{PM}	mass density of the PM
U_3	global displacements of the beam in the z-direction	$v_{BNNT/PM}$	Poisson's ratio of FG-BNNT reinforced PM
u_1	the mid-plane vertical displacements	N_{11}	generalized membrane stress

u_3	the mid-plane axial displacements	M_{11}	generalized bending stress
θ_1	the mid-plane rotation about the y-axis	N_{13}	generalized membrane stress
e_{11}	generalized membrane strain	W_{int}	internal strain energy
κ_{11}	generalized curvature strain	W_f	foundation strain energy
χ_{13}	generalized transverse shear strain	W_{ext}	external work
σ_{11}	axial stress	W_k	kinetic energy
τ_{13}	transverse shear stress	I_0, I_1, I_2	Inertia resultants
		v_{BNNT}	effective Poisson's ratio of BNNT
p_3	transverse sudden dynamic loads	v_{PM}	effective Poisson's ratio of PM
$G_{BNNT/F}$	effective shear modulus of the FG-BNNT-reinforced PM	V_{BNNT}	volume fractions of the BNNT
E_L	axial Young's moduli of the FG-BNNT-reinforced PM	V_{PM}	volume fractions of the PM
E_T	transverse Young's moduli of the FG-BNNT-reinforced PM	V_{CF}	volume fractions of carbon fiber
E_{PM}	Young's moduli of the PM	E_{eff}	Effective Young's moduli of the FG-BNNT/CF-reinforced PM
E_{BNNT}	Young's moduli of the BNNT	G_{eff}	shear modulus of the FG-BNNT/CF-reinforced PM
$E_{BNNT/F}$	Young's modulus	ρ_{eff}	mass density of the FG-BNNT/CF-reinforced PM
W_{BNNT}	weight fraction of the BNNT	v_{eff}	Poisson's ratio of the FG-BNNT/CF-reinforced PM
τ_{13}	transverse shear stress	I_0, I_1, I_2	Inertia resultants

Table 8. List of abbreviations

Abbreviation	Description
FV	forced vibration
PM	polymer matrix
PMCBs	polymer matrix composite material beams
FG-BNNT	functionally graded boron nitride nanotubes
CF	carbon fibers
VEFs	viscoelastic foundations
DMLs	dynamic mechanical loading
BCs	boundary conditions
VWP	Visco-Winkler-Pasternak
FSDT	first-order shear deformation theory
MHTM	modified Halpin-Tsai model
ROM	rule of mixtures
FMM	fiber micromechanics method
HP	Hamilton's principle
FEM	finite element
NITINM	Newmark implicit time integration numerical method

References

[1] Davim JP. Vibration: A bibliometric analysis. Sound & Vibration. 2025;59(2):26-7. https://doi.org/10.59400/sv2627

[2] Davim JP. Modern Mechanical Engineering: Research, Development and Education. Berlin, Heidelberg: Springer; 2014. https://doi.org/10.1007/978-3-642-45176-8

[3] Bhat A, Budholiya S, Raj SA, Sultan MTH, Hui D, Shah AUM, et al. Review on nanocomposites based on aerospace applications. Nanotechnology Reviews. 2021;10(1):237-53. https://doi.org/10.1515/ntrev-2021-0018

[4] Davim JP. Mechanical and Industrial Engineering: Historical Aspects and Future Directions. Springer; 2022. https://doi.org/10.1007/978-3-030-90487-6

[5] Reddy JN. Analysis of functionally graded plates. Int J Solids Struct. 2000;37(50):5159-81. https://doi.org/10.1002/(SICI)1097-0207(20000110/30)47:1/3<663::AID-NME787>3.0.CO;2-8

[6] Davim JP. Composite materials: A bibliometric analysis. AIMSMATES. 2024;11(6):1145-8. https://doi.org/10.3934/matersci.2024055

[7] Merzouki T, Ahmed HMS, Bessaim A, Haboussi M, Dimitri R, Tornabene F. Bending analysis of functionally graded porous nanocomposite beams based on a non-local strain gradient theory. Mathematics and Mechanics of Solids. 2022;27(1):66-92. https://doi.org/10.1177/10812865211011759

[8] Korayem AH, Tourani N, Zakertabrizi M, Sabziparvar A, Duan W. A review of dispersion of nanoparticles in cementitious matrices: Nanoparticle geometry perspective. Constr Build Mater. 2017;153:346-57. https://doi.org/10.1016/j.conbuildmat.2017.06.164

[9] Sadeghi B, Cavaliere PD. Reviewing the integrated design approach for augmenting strength and toughness at macro-and micro-scale in high-performance advanced composites. Materials. 2023;16(17):5745. https://doi.org/10.3390/ma16175745

[10] Ebrahimi F, Dabbagh A. On thermo-mechanical vibration analysis of multi-scale hybrid composite beams. J Vib Control. 2019;25(4):933-45. https://doi.org/10.1177/1077546318806800

[11] Ebrahimi F, Dabbagh A. An analytical solution for static stability of multi-scale hybrid nanocomposite plates. Eng Comput. 2021;37(1):545-59. https://doi.org/10.1007/s00366-019-00840-y

[12] Al-Furjan M, Dehini R, Paknahad M, Habibi M, Safarpour H. On the nonlinear dynamics of the multi-scale hybrid nanocompositereinforced annular plate under hygro-thermal environment. Arch Civ Mech Eng. 2021;21(1):4. https://doi.org/10.1007/s43452-020-00151-w

[13] Ebrahimi F, Nopour R, Dabbagh A, Duc ND. Vibration of three-phase hybrid viscoelastic nanocomposites beams. J Mech Sci Technol. 2023;37(5):2311-7. https://doi.org/10.1007/s12206-023-0407-8

[14] He X, Rafiee M, Mareishi S, Liew K. Large amplitude vibration of fractionally damped viscoelastic cnts/fiber/polymer multiscale composite beams. Compos Struct. 2015;131:1111-23. https://doi.org/10.1016/j.compstruct.2015.06.038

[15] Ahmadi M, Ansari R, Rouhi H. Multi-scale bending, buckling and vibration analyses of carbon fiber/carbon nanotube-reinforced polymer nanocomposite plates with various shapes. Physica E Low-dimensional Syst Nanostruct. 2017;93:17-25. https://doi.org/10.1016/j.physe.2017.05.009

[16] Ebrahimi F, Dabbagh A. Vibration analysis of multi-scale hybrid nanocomposite plates based on a halpin-tsai homogenization model. Compos Part B Eng. 2019;173:106955. https://doi.org/10.1016/j.compositesb.2019.106955

[17] Reyes AN, Tank M, Patadia R, Sweat R. Thermal performance and interply bonding of boron nitride nanotube/carbon fiber hybrid composites. In: SAMPE conference proceedings. Seattle, WA: Society for the Advancement of Materials and Process Engineering; 2023. p. 561-74.

[18] Ebrahimi F, Hosseini SHS. Investigation of flexoelectric effect on nonlinear forced vibration of piezoelectric/functionally graded porous nanocomposite resting on viscoelastic foundation. J Strain Anal Eng Des. 2020;55(1-2):53-68. https://doi.org/10.1177/0309324719890868

[19] Sofiyev AH, Zerin Z, Kuruoglu N. Dynamic behavior of fgm viscoelastic plates resting on elastic foundations. Acta Mech. 2020;231:1-17. https://doi.org/10.1007/s00707-019-02502-y

[20] Younesian D, Hosseinkhani A, Askari H, Esmailzadeh E. Elastic and viscoelastic foundations: A review on linear and nonlinear vibration modeling and applications. Nonlinear Dyn. 2019;97(1):853-95. https://doi.org/10.1007/s11071-019-04977-9

[21] Yang Y, Ding H, Chen L-Q. Dynamic response to a moving load of a timoshenko beam resting on a nonlinear viscoelastic foundation. Acta Mech Sin. 2013;29(5):718-27. https://doi.org/10.1007/s10409-013-0069-3

[22] Fouaidi M, Jamal M, Zaite A, Belouaggadia N. Bending analysis of functionally graded graphene oxide powder-reinforced composite beams using a meshfree method. Aerosp Sci Technol. 2021;110:106479. https://doi.org/10.1016/j.ast.2020.106479

[23] Thostenson E, Li W, Wang D, Ren Z, Chou T. Carbon nanotube/carbon fiber hybrid multiscale composites. J Appl Phys. 2002;91(9):6034-7. https://doi.org/10.1063/1.1466880

[24] Abdollahi I, Yas MH. Free vibration analysis of timoshenko beams reinforced by bnnts and a comparison with cnt-reinforced composite. SN Appl Sci. 2020;2:1-18. https://doi.org/10.1007/s42452-020-2429-5
[25] Dabbagh A, Rastgoo A, Ebrahimi F. Static stability analysis of agglomerated multi-scale hybrid nanocomposites via a refined theory. Eng Comput. 2021;37:2225-44. https://doi.org/10.1007/s00366-020-00939-7
[26] Reddy JN. Theory and analysis of elastic plates and shells. CRC Press; 2006. https://doi.org/10.1201/9780849384165
[27] Zienkiewicz OC, Morice P. The finite element method in engineering science. Vol. 1977. London: McGraw-Hill; 1971.
[28] Reddy JN, Gartling DK. The finite element method in heat transfer and fluid dynamics. CRC Press; 2010. https://doi.org/10.1201/9781439882573
[29] Newmark NM. A method of computation for structural dynamics. J Eng Mech Div. 1959;85(3):67-94. https://doi.org/10.1061/JMCEA3.0000098